Submerged-Plant-Inspired Five-Level-Synergetic hierarchical Single-Fe-Atom-Doped Micro-Electrodes for High-Performance multifunctional electrocatalysis

Yiming Chen [a,1], Yuyang Cai [a,1], Ruohan Yu [a,1], Xuelei Pan [a], Jianyong Zhang [a], Zhaoyang Wang [a], Xiao Xiao [a], Jinsong Wu [a], Lin Xu [a,b,*], Liqiang Mai [a,b,*]

[a] State Key Laboratory of Advanced Technology for Materials Synthesis and Processing, Wuhan University of Technology, Wuhan 430070, China
[b] Foshan Xianhu Laboratory of the Advanced Energy Science and Technology Guangdong Laboratory, Xianhu hydrogen Valley, Foshan 528200, China

ARTICLE INFO

ABSTRACT

Multifunctional electrocatalyst delivers powerful ability in energy storage and conversion systems to relieve energy crisis nowadays. However, due to the complexity of material synthesis and electrode construction, it still remains a challenge to achieve multifunctionality while maintaining high catalytic activity. In this work, inspired by the unique structure of submerged plants, three dimensional hierarchical electrodes were constructed via 3D printing and applied in water splitting devices and Zn-air batteries to emulate the photosynthesis and respiration, respectively. The fabricated electrodes possess surface single-Fe-atom-doped $Ni/Ni(OH)_2$ and embedded Fe-doped carbon nanotubes (Fe-CNTs), which contribute to water splitting and oxygen reduction reaction (ORR), respectively. Benefiting from the hierarchical synergetic structure and appropriate location of active center, overpotentials of 175 mV and 108 mV were respectively achieved for oxygen evolution reaction and hydrogen evolution reaction to reach 30 mA cm^{-2} in 1 M KOH solution, and corresponding overall water splitting required a low voltage of 1.51 V. In addition, the assembled Zn-air battery achieved a power density of 143.8 mW cm^{-2}. Overall, the fabricated 3D electrodes presented remarkable potential for overall water splitting and Zn-air batteries, and this strategy also put forward a new avenue for designing and constructing high-performance trifunctional electrocatalyst electrodes.

1. Introduction

The continuous consumption of fossil fuels promoted the development of energy storage and conversion devices [1]. Among energy conversion systems, electrocatalysis of producing H_2 by water splitting is a popular and efficient route [2]. Decreasing the overpotential of oxygen evolution reaction (OER)/hydrogen evolution reaction (HER) and increasing the corresponding catalytic stability are the main directions to promote the efficiency of water splitting [3]. Relevant strategies include designing active sites to reduce the reacting energy barrier [4–9], constructing three dimensional (3D) electrodes to increase the exposed area [10,11] and configuring channels for the efficient release of produced gas bubbles [12–14]. Among energy storage devices, rechargeable metal-air battery delivered unique application potential

due to its high energy density, low cost and high stability [15–17]. As a crucial strategy, optimizing the catalyst in cathode plays a vital role in promoting the energy efficiency (input/output voltage) and cycling stability. Designing active sites for OER and oxygen reduction reaction (ORR) is critical to reduce reacting energy barrier and further elevate the energy efficiency of rechargeable metal-air batteries [18–21]. Furthermore, constructing individual diffusion channels for O_2 and electrolyte will construct abundant three-phase interface and optimize operating properties under large current densities [22–26].

As mentioned above, fabricating electrodes with high electrocatalytic performance was widely explored, however, it still remains a challenge to intelligently integrate multifarious catalytic active sites into a single electrode [27–29]. Since electrocatalysis usually requires multi kinds of catalytic ability when applied in overall water splitting (OWS)

and metal-air batteries, it brings forward high request for the catalyst to combine multifunctional catalytic ability, which will considerably simplify the system and decrease the cost. In addition, in order to make the composite catalyst "keep its place and perform its duty", the constructed electrodes are highly demanded to possess proper configuration to make the best use of each kind of active sites and gain optimized multifunctional catalytic abilities.

Submerged plant is a kind of ordinary plant living in water (shown in Fig. 1a), which usually possess hierarchical branches/leaves and inner porous stems to adapt to the environment with dim sunlight and thin O_2/CO_2 [30]. As shown in Fig. 1b, during photosynthesis, dense branches/leaves with large surface area act as the sunshine collector which transfer H_2O and CO_2 into O_2 and biomass [31]; during respiration, hollow stems provide unique channels to transport O_2 to the whole plant body and supply nourishment for each cell. In this work, inspired by the production and transport of O_2 in photosynthesis and respiration of submerged plant, 3D hierarchical electrodes were fabricated by 3D-printing process (Fig. 1c) to boost the properties both in water splitting and Zn-air battery. In the experiment, a facile "ion exchange" strategy was developed to construct this high-performance trifunctional catalyst electrode: Fe source in the Fe-CNTs acted as crucial role for ORR process, and also provided the doped Fe in promoting the OER/HER performance of loaded $Ni/Ni(OH)_2$. As shown in Fig. 1d, the constructed multi-scale hierarchical structure offered large exposed area to electrolyte and facilitated the release of produced gas bubbles (refer to photosynthesis), and the 3D hollow structure provided individual paths for the transport of O_2 and electrolyte (refer to respiration). As a result, the electrodes exhibited low overpotentials for OER and HER, as well as low voltage for overall water splitting. In addition, the assembled Zn-air battery also presented considerable performance. Finally, this bio-inspired 3D hierarchical structure and constructed multi-scale-synergetic configuration show promising potential in practical application and put forward a new strategy for developing high-performance trifunctional catalytic electrode.

2. Experiment section

2.1. Preparation of hydrogel ink

Cellulose Nanofiber (CNF), bacterial cellulose (BC) and dicyandiamide were utilized as the additive to prepare the printable ink. CNF and BC suspension (mass concentration: 2%) was purchased from Qihong company. Firstly, 2% dicyandiamide was dissolved into the BC suspension by stirring for 30 mins. Afterwards, 5% CNF was added into BC/dicyandiamide suspension followed with continuous stirring (under a

speed of 3000 rpm, SpeedMixer^{TM} DAC 150.1 FVZ) until a semi-transparent hydrogel ink was obtained.

2.2. 3D-printing process

The prepared ink was extruded and stacked obeying the designed 3D model by 3D printer (Cellink^{TM}, BIO-X) under 470 kPa with a speed of 15 mm s^{-1}. Then, the constructed 3D hydrogel was freeze-dried (-40 °C) and carbonized (keep 800 °C for 2 h, with a heating rate of 5 °C min^{-1}) into a 3D carbon-based framework (denoted as 3DC).

2.3. The growth of CNTs

The 3DC was immersed into 0.1 M $Fe(NO_3)_3$ solution for 15 mins. Afterwards, it was freeze-dried to remove water and remained Fe salt was absorbed on the framework. Then, the modified sample was carbonized at 900 °C (keep for 2 h, with a heating rate of 5 °C min^{-1}) with a flowing melamine vapour (melamine was put in front of the sample following the airflow). After cooling down to room temperature, Fe-CNTs were successfully grown on the carbon-based framework. Co-CNTs and Ni-CNTs were grown in the same method except that Fe $(NO_3)_3$ solution was replaced by $Co(NO_3)_2$ and $Ni(NO_3)_2$ solution (the same concentration), respectively.

2.4. Preparation of loaded Ni/Ni(OH)$_2$

The 3DC-Fe-CNTs framework was electro-deposited with Ni referring to the reported strategy [32–34]: −6 V bias voltage (vs saturated calomel electrode using a three-electrode system) was applied to the electrodes in the electrolyte (0.1 M $NiSO_4$, 2 M NH_4Cl and 2 M NaCl) and lasted for 150 s. It is worth mentioning that, fabricated electrodes were fixed by titanium network to conduct plating and tests, and before electrodeposition, immersion of 30 mins was conducted to dissolve Fe (on CNTs) into the electrolyte. The obtained 3DC-Fe-CNTs-Ni framework was anodized in 1 M KOH solution under a current density of 100 mA cm^{-2} for 1 h (with a new titanium network used). Finally, 3D electrode of 3DC-Fe-CNTs-Ni/Ni(OH)$_2$ was obtained (denoted as CFCNN). Electrode of 3DC-Ni/Ni(OH)$_2$ was also fabricated except the growth of Fe-CNTs (denoted as 3DC-NN). Electrodes of 3DC-Ni-CNTs-Ni/Ni(OH)$_2$ (denoted as 3DC-Ni-CNN) and 3DC-Co-CNTs-Ni/Ni(OH)$_2$ (denoted as 3DC-Co-CNN) were fabricated using the same electrodeposition and anode oxidation process.

2.5. Preparation of catalytic inks

Prepared 3DC-Fe-CNTs and 3DC-Fe-CNTs-Ni/Ni(OH)$_2$ were ground into powders. 5 mg powder of active material, 5 mg conductive carbon (72-R), 800 μL isopropyl alcohol, 150 μL deionized water and 50 μL nafion solution (5 wt.%) were mixed and sonicated for 1 h until well-proportioned catalytic ink was obtained. The same method was used to prepare Pt-C&RuO$_2$ ink.

2.6. Materials characterization

Scanning electron microscope (SEM) was performed using a JEOL-7100F field-emission SEM (acceleration voltage: 20 kV). Transmission electron microscope (TEM) was conducted employing a Titan G2 60–300 Probe Cs Corrector HRSTEM. X-ray diffraction (XRD) was recorded via a D8 discover X-ray diffractometer with Cu Kα radiation. Raman tests were carried out using a HORIBA HR EVO Raman system. X-ray photoelectron spectroscopy (XPS) spectra were recorded using a VG Multilab 2000. The X-ray absorption spectra (XAS) including X-ray absorption near-edge structure (XANES) and extended X-ray absorption fine structure (EXAFS) of the sample at XX-edge was collected at the Beamline of TLS07A1 in National Synchrotron Radiation Research Center (NSRRC), Taiwan. The Scanning transmission electron
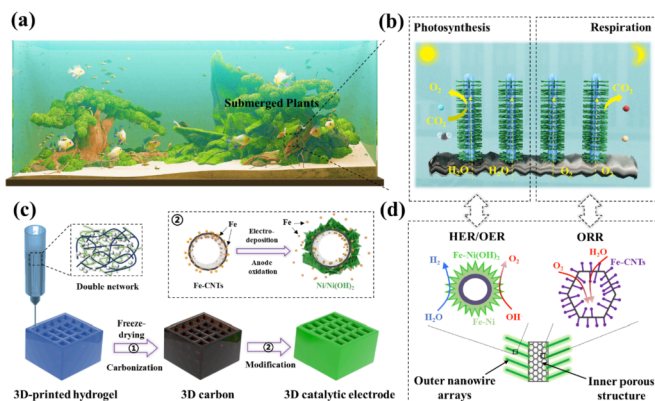
Fig. 1. Schematic illustration: (a) Submerged plants in water. (b) Photosynthesis and respiration process of submerged plants. (c) Fabricating process of the 3D electrode and relevant doping mechanism of Fe atoms. (d) H_2/O_2 release channels in the sample during OER/HER processes and reacting path of O_2 during charge/discharge in Zn-air batteries.

microscope (STEM) characterization was performed on a Thermo Fischer Titan Themis STEM with 300 kV acceleration voltage. The STEM images were obtained by an annular bright field (ABF) detector and a high angle annular dark field (HAADF) detector, respectively. Fe content was tested using an Elemental Analyzer (Model: Vario EL cube).

2.7. Electrochemical tests

All of the electrochemical tests were conducted using an CHI760D electrochemical workstation at room temperature. All of the linear scan voltammograms (LSVs) tests were conducted at the scan rate of 5 mV s^{-1}. OER was tested using three-electrode system (vs. Hg/HgO reference electrode, Pt plate with the area of 1 cm^2 as the count electrode) in 1 M KOH solution. HER was tested using three-electrode system (vs. Hg/HgO reference electrode, graphite rod with a diameter of 8 mm as the count electrode) in 1 M KOH solution. OWS was conducted using a two-electrode system in 1 M KOH solution. Chronopotentiometry measurements were performed to evaluate the stability of water splitting. Double-layer capacitance (C_{dl}) was obtained by conducting the cyclic voltammetry (CV) tests under the potential window from 0 to 0.1 V vs. Hg/HgO electrode. The scan rates were 1, 2, 5, 8, 10 mV s^{-1}. C_{dl} was estimated by plotting the $\Delta J = (J_a - J_c)$ at 0.05 V vs. Hg/HgO against the scan rate, and the linear slope is twice of the C_{dl}. ORR was tested via a rotating disk electrode (area = 0.196 cm^2) using three-electrode system (vs. Hg/HgO reference electrode, Pt as the count electrode) in 0.1 M O_2 saturated KOH solution. Water splitting results were presented after 90% IR compensation. All potentials tested by Hg/HgO reference electrode were converted to potentials vs. reversible hydrogen electrode (RHE) according to $E_{RHE} = E_{Hg/HgO} + 0.059 \times pH + 0.098$.

3. Results and discussions

As investigated by previous researchers, some hydrogel owns proper rheological property for 3D printing [35,36]. In this work, CNF, BC and dicyandiamide were employed as the ingredients (Fig. S1, see **Experiment section** for details). CNF acted as the additive to increase the storage modulus of the ink since abundant oxygen-containing functional groups brought abundant hydrogen bonds by interacting with water molecules [37,38]. BC is cellulose fiber with large length/diameter ratio, which acted as 3D interconnected network to reinforce the obtained frameworks [39,40]. Dissolved dicyandiamide is the N-containing source to load Fe catalyst, and the derived pyrolysis carbon will increase the durability of this carbon-based scaffold during water splitting process. After dispersed into water, semitransparent hydrogel was obtained. The rheological property of prepared hydrogel was shown in Fig. S2, which exhibits a typical shear-thinning and non-Newtonian-fluid property [37,41,42], and the inset digital photograph of prepared hydrogel in Fig. S2a declared its homogeneous property. The schematic illustration of the fabricating process was shown in Fig. S3. After piling up into a 3D structure, the hydrogel can maintain a fine configuration (see Video 1), which manifests the gelation effect of CNF and the reinforcement of BC. After freeze-drying, the constructed 3D hydrogel was transferred into a white scaffold. Followed by a carbonization process, a shrunken 3D carbon-based framework (denoted as 3DC) was obtained, corresponding SEM images were shown in Fig. S4. Rough surface of the carbon flakes (Fig. S4 a, b) and inner porous configuration (Fig. S4 c, d) can be identified, which will serve as the porous 3D scaffold to support the following loaded active materials.

After immersed into Fe(NO₃)₃ solution and freeze-dried, ferric salt was adsorbed on the fabricated 3DC. When further annealed in the flowing melamine steam, adsorbed Fe acted as the catalyst and triggered the growth of Fe-doped carbon nanotubes (Fe-CNTs) [43,44]. The samples modified by Fe-CNTs can be observed in Fig. S5, in which 3DC-Fe-CNTs framework (denoted as CFC) shows the same dimensions as 3DC. The length of Fe-CNTs varies from 5 to 100 μm and the average diameter is around 100 nm. As shown in Fig. S5b, c, it is evident that Fe-

CNTs grown in different directions, indicating abundant defects and edges existed in Fe-CNTs, which facilitated the dissolution of Fe into the electrolyte during the following electrodeposition process. In the TEM images (Fig. S6), Fe particles can be found both in the endpoint and middle of the Fe-CNT. In the high magnification TEM image (Fig. S6d), crystal structure with d-spacing of 0.203 nm can be observed and it can be indexed to the (1 1 0) plane of Fe (JCPDS No. 00–006-0696) [45]. On the surface of Fe particle, layered materials can be observed (d = 0.34 nm), which is identified as the wall of the CNT [46]. The agglomerated Fe particles and uniformly dispersed Fe can be both identified in energy-dispersive X-ray spectroscopy (EDS) mapping images of Fe-CNTs (Fig. S7), among which uniformly dispersed Fe on Fe-CNTs will contribute to the ORR process in the following assembled Zn-air batteries. The XRD and Raman curves were shown in Fig. S8, among which the XRD curve (Fig. S8a) exhibited characteristic peaks of CNTs and Fe, and typical D band and G band can be observed in the Raman curve (Fig. S8b) [45].

After electrodeposition and anode oxidation process, 3DC-Fe-CNTs-Ni/Ni(OH)₂ (denoted as CFCNN) electrode was obtained, the finely constructed 3D electrode was shown in the inset of Fig. 2a. The loaded Ni/Ni(OH)₂ nano-sheets vertically aligned due to the assistance of bubble template during the electro-plating process, and the surface morphology was show in Fig. 2a-c. Judging from Fig. 2c, dense Ni/Ni(OH)₂ nano-sheets are located on the surface of Fe-CNTs. STEM and corresponding EDS mapping results were shown in Fig. S9, CNT was finely covered by Ni/Ni(OH)₂ nano-sheets and obvious dispersion of Fe can be identified all over the material. To clearly observe the structure of Fe-CNTs-Ni/Ni(OH)₂, rotating STEM was conducted. The recorded video was shown in Video 2, in which bright particles (Fe) can be identified on the surface of CNT and nano-sheets of Ni/Ni(OH)₂ were arrayed on the surface.

In the cross-sectional SEM image of the CFCNN electrode (Fig. 2d), honeycomb-like structure can be observed, which resulted from the ice-template process. To clearly observe the located region of Ni/Ni(OH)₂, EDS mapping tests were conducted (shown in Fig. 2e and Fig. S10, Fig. S11). In these SEM and corresponding EDS mapping results under different magnifications, clear boundary lines between Ni and C can be observed. In addition, Ni element located mainly in the outer surface of the CFCNN electrode and C element mainly appeared in the inner space. The cause was judged to be that, during the electrodeposition process, Ni preferentially deposited on the outer surface (more fully exposed to electrolyte), and the inner CNTs almost still remained uncovered. Signal related to Fe element was dispersed all over the whole electrode, which is judged to be resulted from two routes: (1) the remained Fe particles in CNTs; (2) some exposed Fe species were dissolved into the Ni-based electrodeposition electrolyte (by replacement reaction with Ni^{2+}) and dissolved Fe^{2+} ions were redeposited on the electrode under the applied bias voltage. The high-magnification cross-sectional SEM image of the inner region in the electrode was shown in Fig. 2f, in which relatively smooth CNTs can be identified. In addition, the corresponding HAADF and related EDS mapping result (Fig. 2g, EDS was shown in Fig. S12) also indicated that the CNTs were almost uncovered by Ni/Ni(OH)₂, which will provide exposed Fe-CNTs to facilitate ORR process in Zn-air batteries. The pore configuration of the electrode was investigated by N_2 adsorption–desorption isotherms (Fig. S13). The isotherm (Fig. S13a) exhibited IV type, and the Brunauer–Emmett–Teller (BET) surface area is 187 m^2/g. Pores are mostly mesopores and macropores, in which the width was mostly in the range of 2–4 nm and 10–100 nm (Fig. S13b). The former was possibly resulted from pyrolysis carbon and the latter may reflect the CNTs networks.

XRD measurement was performed to determine the composition and corresponding phase. As defined in Fig. S14, peaks related to Ni (JCPDS No. 01–089-7128) and Ni(OH)₂ (JCPDS No. 00–014-0117) can be identified, and the peak at around 26.6° refers to the graphite carbon in CNTs, which demonstrate the coexistence of Ni, Ni(OH)₂ and graphite carbon. XPS tests were conducted to declare the composition and
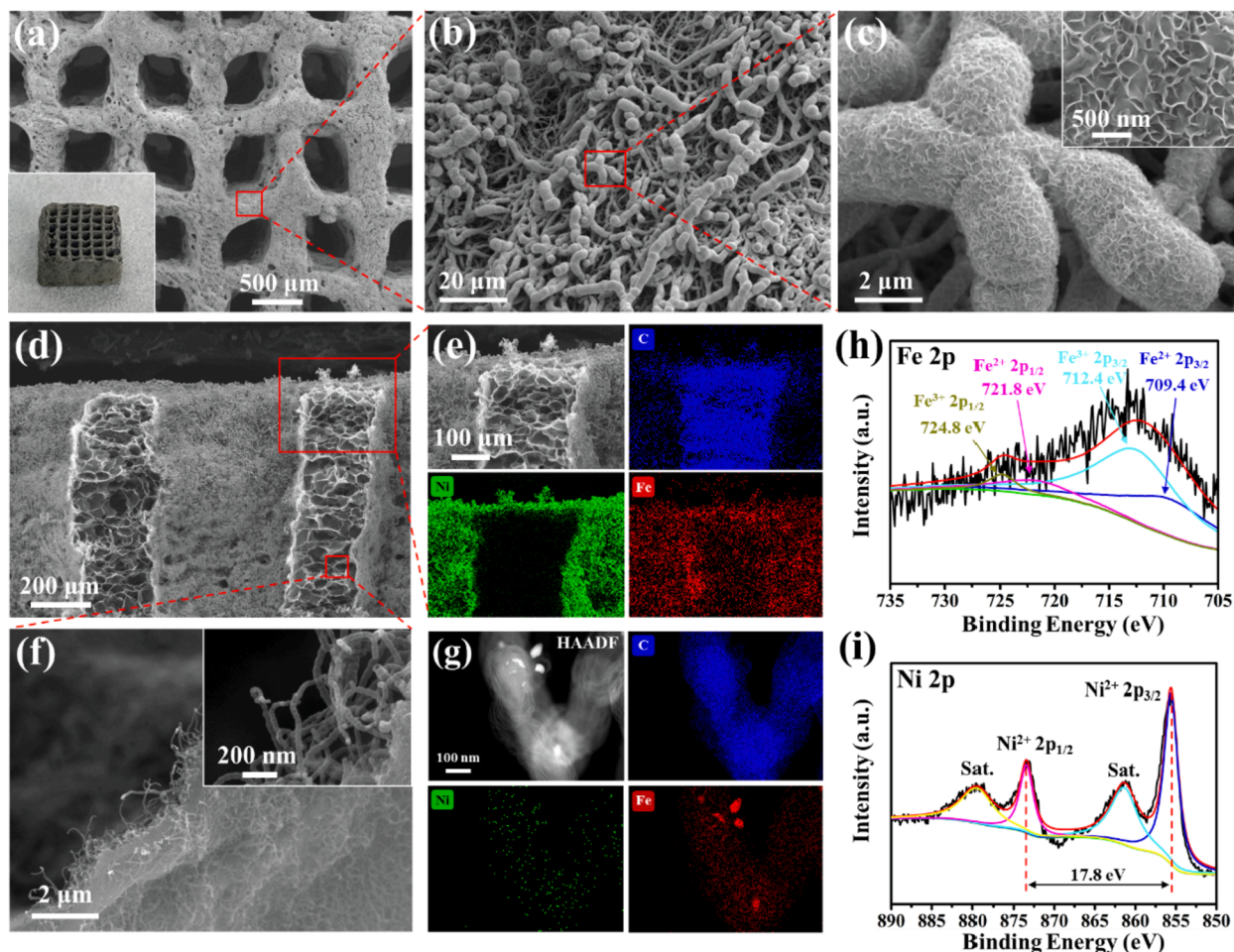
Fig. 2. (a-c) Top-view and (d) cross-sectional SEM images of the fabricated 3D electrodes. Insert of (a) is the digital photograph of fabricated 3D electrode. (e) Selected area of the cross-sectional SEM image and related EDS mapping result of C, Ni and Fe. (f) Magnified SEM image of the inner region of the CFCNN electrode, inset shows the embedded CNTs. (g) HAADF image of inner CNT and corresponding EDS mapping results of C, Ni and Fe. High magnification XPS curve of (h) Fe 2p and (i) Ni 2p for CFCNN electrode.

chemical state of the prepared samples, recorded curve was shown in Fig. S15. Obvious peaks can be identified which confirmed the coexistence of C, O, N, Ni and Fe element [13,45,47–49]. The deconvolution peaks of Fe 2p (Fig. 2h) indicated the presence of bivalent (709.4 and 721.8 eV) and trivalent (712.4 and 724.8 eV) Fe, manifesting that some Fe existed in oxidized state [47]. Two typical peaks at 873.4 and 855.6 eV can be identified in Ni 2p high-resolution spectrum (Fig. 2i), which are in accordance with Ni $2p_{1/2}$ and Ni $2p_{3/2}$ levels, respectively. This spin-energy separation of 17.8 eV is also the characteristic of $Ni(OH)_2$ phase, consistent with the reported results [48,50].

Micro-region analysis was conducted by aberration-corrected STEM coupled with electron energy loss spectrum (EELS) test to detect the element dispersion and chemical environment of Fe and $Ni/Ni(OH)_2$. Judging from the selected region of $Ni/Ni(OH)_2$ nano-sheet and corresponding EELS mapping results (Fig. 3a), the dispersion of Fe was highly consistent with Ni and O in the selected area, and the alternating light and dark mapping result of Fe element indicated that Fe was well dispersed and might exist in the form of single atom. After background subtraction, corresponding EELS curves were shown in Fig. 3b and Fig. S16, in which peaks related to O K edge, Fe $L_{2, 3}$ edge and Ni $L_{2, 3}$ edge can be observed [51,52], further demonstrating the coexistence of Fe, Ni and O element [51]. To clearly investigate the contents of Fe, Ni and O in the $Ni/Ni(OH)_2$ nano-sheet, different area was selected to measure the detailed content (abbreviated as Cont.), shown in Fig. S17a. Recorded spectra were shown in Fig. S17b. In all of selected area, evident peaks related to O K edge, Fe L edge and Ni L edge can be

observed, and detailed Cont. of the whole region and selected Region 1–4 are listed in Table S1. The Cont.$_{Fe}$ in Region 1–4 are all between 1.8% and 2.6%, declaring the uniform and effective doping of Fe. To investigate the total Cont.$_{Fe}$ in the fabricated 3D CFCNN electrode, inductively coupled plasma mass spectrometry (ICP–MS) test was conducted and the recorded Cont.$_{Fe}$ was 4.15%. Cont.$_{Fe}$ in $Ni/Ni(OH)_2$ nano-sheet was relatively lower than the whole electrode, which can be ascribed to that, some Fe particles remained on CNTs, and they contributed to a larger proportion of Cont.$_{Fe}$ in the whole electrode.

In the ABF (Fig. 3c) and HAADF (Fig. 3d) graphs from STEM test, atomic images can be observed. The lattice plane distance of the layered structure was measured to be 0.233 nm, which was indexed to be (1 0 1) lattice plane of $Ni(OH)_2$ (JCPDS No. 00–014-0117) [48], the corresponding lattice structure was also finely matched (shown in the bottom-right-corner inset image of Fig. 3d and Fig. S18). In the bottom-right-corner inset image of Fig. 3d, some atoms in dark contrast can be observed (yellow circled), which might be atomically dispersed Fe (contrast signal image was shown in the top-right-corner inset image of Fig. 3d). EDS mapping result of $Ni/Ni(OH)_2$ nano-sheet was shown in Fig. S19, in which (1 0 1) plane of $Ni(OH)_2$ (d = 0.233 nm) and (1 1 1) plane of Ni (d = 0.203 nm) can be identified, and the dispersion of Fe was also in accordance with Ni and O, further demonstrating the uniform doping of Fe into $Ni(OH)_2$.

To further verify the chemical state of incorporated Fe atoms, synchrotron X-ray absorption fine structure (XAFS) at Fe K-edge was conducted (Fig. 3e). In XANES (Fig. 3f), the absorption edge of CFCNN is
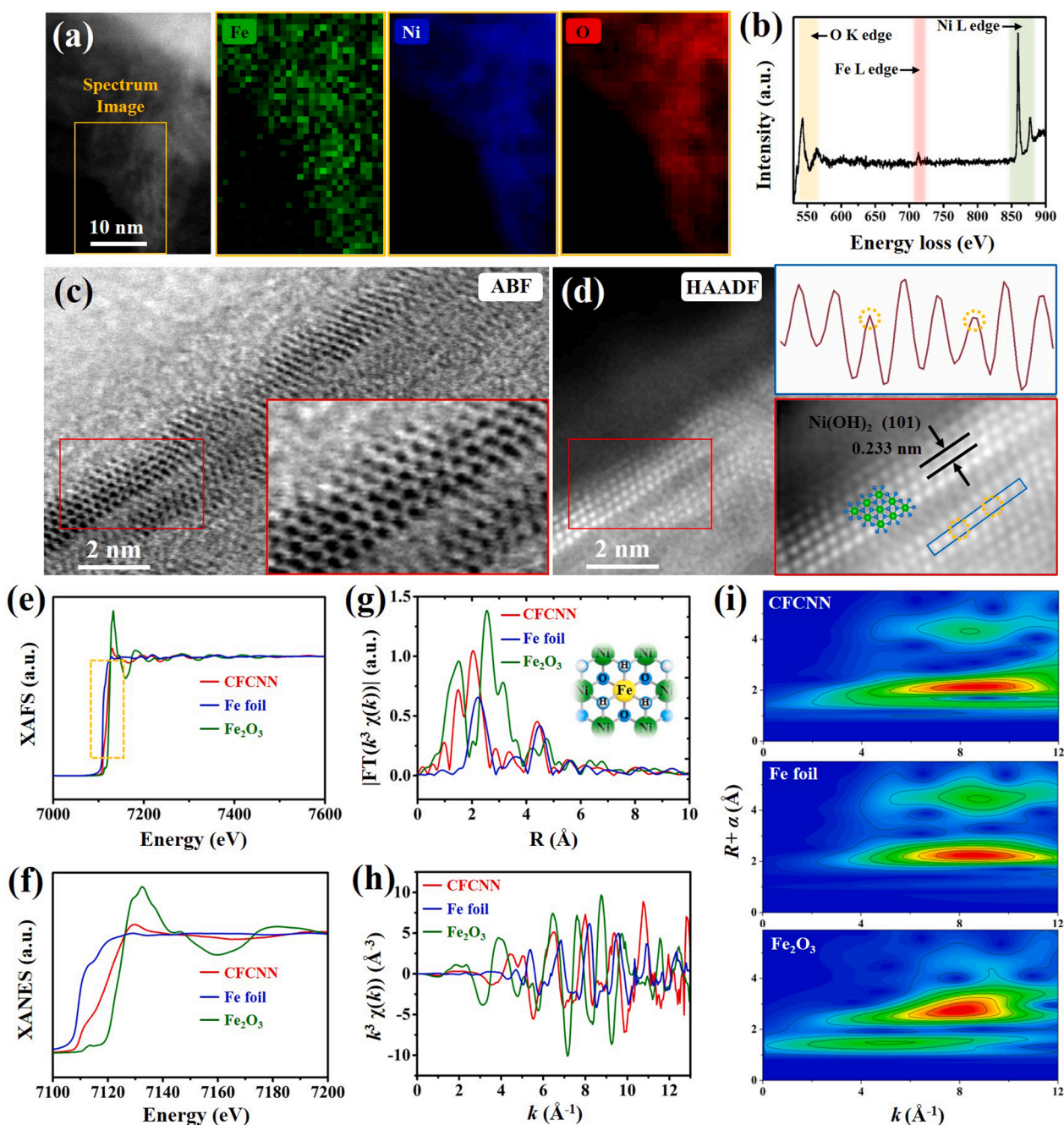
Fig. 3. (a) HAADF image of a selected region of $Ni/Ni(OH)_2$ nano-sheet and corresponding EELS mapping results of Fe, Ni and O. (b) EELS curve of the selected area. (c) The ABF and (d) HAADF image of the STEM test. Bottom-right-corner inset of (d) shows the magnified atomic image and top-right-corner inset shows the contrast signal of selected atoms. (e) The XAFS curves, (f) XANES curves, (g) R space of the Fourier transform from k space, (h) k space of EXAFS results and (i) WT images of CFCNN, Fe foil and Fe_2O_3.

between Fe foil and Fe_2O_3, indicating the valence state is between 0 and + 3 [53]. EXAFS was collected to determine the distance between Fe atoms and further confirm the coordination configuration. The Fourier-transformed (FT) k^3-weighted EXAFS spectra including Fe foil and Fe_2O_3 were shown in Fig. 3g. Compared with Fe foil, similar Fe-Fe shell peak at 2.2 Å and 4.6 Å can be identified in CFCNN [54], which was resulted from two different Fe-Fe distance in Fe particles from Fe-CNTs. Furthermore, the peak corresponding to Fe-O in CFCNN curve can be identified (1.6 Å, consistent with that of Fe_2O_3) and no peak related to Fe-Fe distance in Fe_2O_3 (2.8 Å) can be found, indicating there was no Fe_2O_3 particle in the sample but Fe-O bond existed. In addition, no peak appeared related to bond distance larger than 4.6 Å, indicating no

oxidized-state Fe particle (such as $Fe(OH)_3$, $Fe(OH)_2$, FeO, etc.) existed. The k space was shown in Fig. 3h and corresponding Wavelet transform (WT) was also conducted (shown in Fig. 3i) to investigate the Fe K-edge EXAFS oscillations. At about 8 Å^{-1}, evident peaks can be observed in CFCNN (two peaks respectively at 2.2 Å and 4.6 Å), Fe foil (two peaks at 2.2 Å and 4.6 Å) and Fe_2O_3 (one peak at 2.8 Å), corresponding to the closest or next-closest neighbouring Fe atoms. At around 5.2 Å^{-1}, evident peak in Fe_2O_3 and broad peak in CFCNN (both at 1.6 Å) can be identified, which reflected the neighbouring O atom [53–56]. Combining with the micro-region analysis of STEM, we can draw a conclusion that, the Fe was doped into $Ni/Ni(OH)_2$ in the single-atom form and coordinated with O atom in $Ni(OH)_2$ (detailed configuration

was shown in the inset of Fig. 3g and Fig. S18). According to the reported results, the doping of single-atom Fe in Ni/Ni(OH)$_2$ will play a significant role in promoting the performance of water splitting [57,58].

From above characterization results, it is convictive that the incorporated Fe located both in the Fe-CNTs and Ni/Ni(OH)$_2$. This demonstrated that, the annealing and electrodeposition process successfully incorporated Fe source into 3DC framework and deposited Ni/Ni(OH)$_2$, respectively. For the cause of atomically dispersed Fe in Ni/Ni(OH)$_2$, we estimated that: when Fe-CNTs loaded electrodes were immersed in Ni(NO$_3$)$_2$-based solution during electrodeposition process, some exposed Fe particles were replaced by Ni^{2+} and dissolved into the solution. After applied a bias voltage (-6 V vs. Hg/HgO), the dissolved Fe^{2+} ions were redeposited on CFC substrate together with Ni^{2+} ions. In the electrolyte, the content of Fe^{2+} is much lower than Ni^{2+}, thus we can obtain single-Fe-atom-doped Ni metal after the uniform electrodeposition process. After anode oxidation, they were converted into single-Fe-atom-doped Ni/Ni(OH)$_2$.

To evaluate the electrocatalytic performance, we investigated the OER and HER performance of the CFCNN electrodes in 1 M KOH using a standard three-electrode system (vs. Hg/HgO electrode). Fabricated electrodes with the thickness of 2, 3 and 4 mm were fixed by titanium network (Fig. S20) and respectively tested, Fig. 4a-c show the evolution process of O$_2$ and H$_2$. Recorded linear sweep voltammetry (LSV) curves compared with Pt-C/RuO$_2$ were shown in Fig. 4d, f. Among the electrodes in different thickness, 4 mm electrode exhibited the highest performance: it exhibited overpotentials of 175 mV and 108 mV to reach a current density of 30 mA cm^{-2} for OER and HER, respectively, and only acquire a low overpotential of 233 mV (OER) and 164 mV (HER) to achieve 100 mA cm^{-2}, manifesting its high water electrocatalytic efficiency (Fig. 4d, f). Compared with the benchmark OER electrocatalyst RuO$_2$, the performance of CFCNN electrodes delivered great advantage, shown in Fig. 4d. The simulated Tafel plots of electrodes of 2, 3 and 4

mm for OER and HER are shown in Fig. 4e, g, in which the CFCNN-4 mm electrode exhibited low Tafel slop of 47 mV dec^{-1} for OER and 91 mV dec^{-1} for HER. Considering the high performance of OER and HER, two CFCNN-4 mm electrodes were assembled into a symmetric OWS vehicle and the LSV curve was shown in Fig. 4h. This OWS vehicle exhibited a low voltage of 1.51 V to achieve a current density of 30 mA cm^{-2}, 1.71 V to reach 100 mA cm^{-2} and 2.05 V to reach 1 A cm^{-2} (much better than Pt-C//RuO$_2$). In terms of the practical splitting efficiency and relevant stability, this OWS vehicle can work under 30 mA cm^{-2} stably longer than 10 h (Fig. 4i). When operated under 1 A cm^{-2}, the vehicle exhibited a stable voltage demand around 1.9 V longer than 10 h (Fig. 4i), which demonstrated its industrialized application potential. The chemical state of the samples after 10 h OER/HER tests was characterized, corresponding XPS curves of Ni 2p and Fe 2p were shown in Fig. S21. After OER test, the 2p$_{1/2}$ and 2p$_{3/2}$ peaks of Ni and Fe both exhibited positive shift, which manifested the elevated valence of Ni and Fe species in the sample. Significantly, peaks of Ni^{3+} at 856.7 and 874.6 eV can be observed (Fig. S21a) after OER test [59], which indicated the formation of NiOOH during the reaction. In addition, as shown in Fig. S21b, the positive shift of Fe 2p peaks after OER test also indicated the increase of Fe^{3+} proportion (at 712.4 and 724.8 eV, respectively) in the sample [59]. After HER test, the binding energy of Ni 2p and Fe 2p remained almost unchanged, which indicated the relatively stable chemical state during the HER state.

To estimate the electrocatalytic ability of the fabricated CFCNN-4 mm electrode, the overpotentials of OER/HER and voltage of OWS (at 30 mA cm^{-2}) were compared with some representative reported results which used 3D electrodes with high surface area and hierarchical microstructure (shown in Fig. 4j) [11,60–77], indicating that the performance was better than most of the listed works.

To reveal the significance of the prepared 3D electrodes, including high mass-loading of active materials, hierarchical porous structure,
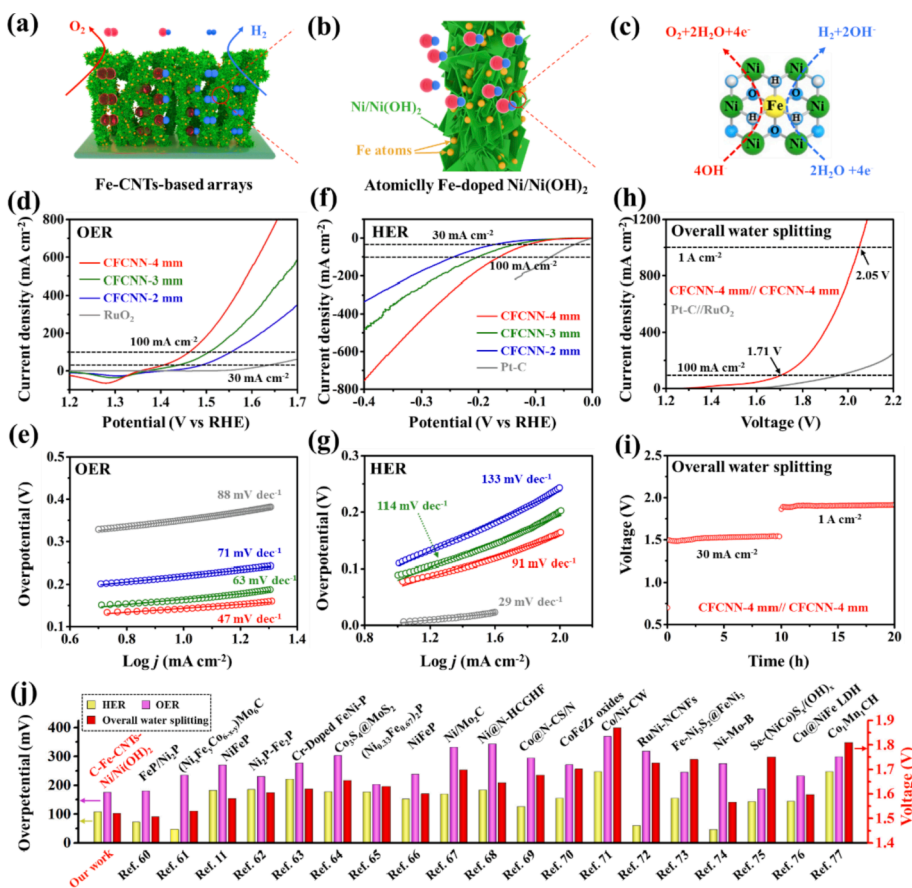
Fig. 4. (a-c) The schematic illustration of water splitting and the significance of the hierarchical structure during the splitting process. (d) The OER LSV curves and (e) corresponding Tafel plots of CFCNN electrodes with different thickness compared with RuO$_2$ catalyst. (f) The HER LSV curves and (g) corresponding Tafel plots of CFCNN electrodes with different thickness compared with Pt-C catalyst. (h) The LSV curves of OWS by CFCNN-4 mm//CFCNN-4 mm compared with Pt-C//RuO$_2$. (i) The stability test result of above OWS vehicle under 30 mA cm^{-2} and 1 A cm^{-2}. (j) Comparison of the overpotentials of OER/HER and voltage of OWS with representative published works.

surface nanowire arrays, total high conductivity and single-Fe-atom doping, control experiments were conducted, relevant results and analysis were shown in Fig. S22-26. In addition, since the release of generated gas bubbles is one of the most important rate-determining steps for the water splitting process, in-situ observation through a home-made optical microscope vehicle was conducted and the recorded process (0.6 V vs. Hg/HgO was applied) was shown in Video 3. During this OER process, small bubbles rapidly broke away from the surface of electrode before their aggregation, and smoothly passed through the 3D printed channels along a short vertical pathway. The observed rapid release of gas bubbles revealed the significance of the 3D-printed periodic pores, which provided efficient transport channels.

Above comparison and recorded video revealed the following significance of the constructed 3D CFCNN: (1) CFCNN-4 mm with customized thickness and regulated surface area brought higher-mass-loaded active materials and achieved higher reacting efficiency in a foot-print area (contrast with 3DC-NN and P-CFCNN); (2) Hierarchical porous structure provided multi-scale effusion channels for produced H_2/O_2 and accelerated the mass transportation of electrolyte ions (contrast with Bulk-CFCNN); (3) The relatively vertically aligned Fe-CNTs-Ni/Ni(OH)$_2$ nanowire arrays exhibited relatively aerophobic property and facilitated the release of produced H_2/O_2 bubbles from the surface of electrodes (contrast with 3DC-NN); (4) 3DC-supported Ni framework provided high electronic conductivity and the electrode exhibited high performance even under large current densities (contrast with P-CFCNN); (5) Single-Fe-atom doping regulated the electronic structure of Ni/Ni(OH)$_2$ and immensely optimized the OER performance.

Inspired by the transport of O_2 in the stem of submerged plant, CFCNN electrode was assembled into Zn-air batteries (Fig. 5a). The detailed configuration of this customized Zn-air battery was shown in Fig. S27, in which two parallel plastic boards provided the pressure force and inner spring supplied resistance force, and the 3D CFCNN electrode can be finely anchored. As clarified in Fig. 5b, c, the fabricated CFCNN electrode was expected to offer separated and unique reacting environment for OER and ORR: Fe-CNTs-Ni/Ni(OH)$_2$ nanowires on the outer surface were fully exposed to electrolyte and inner honeycomb-like scaffold can simultaneously facilitate the diffusion of O_2 and electrolyte (Fig. 5b). During charging process, the single-Fe-atom-doped Ni/(OH)$_2$ supplied large-area two-phase interface and delivered high catalytic ability for OER. During discharging process, in the inner porous structure (pore diameter of ~ 10 μm), the invasive O_2, partly permeated electrolyte and inner Fe-CNTs supplied large-area three-phase interface (between O_2, H_2O and catalyst), and exhibited high efficiency for ORR (Fig. 5c). After assembled into Zn-air battery, recorded charging and discharging curves were shown in Fig. 5d. Compared with Zn-air battery powered by Pt-C&RuO$_2$ and P-CFCNN catalyst, the electrode exhibited higher current densities both in charging and discharging process. Calculated from the output voltage and corresponding current densities, the power density was shown in Fig. 5e. This device can yield high power density of 143.8 mW cm^{-2} under 378.4 mA cm^{-2}, exceeding that of Pt-C&RuO$_2$ catalyst (maximally yield 88.2 mW cm^{-2} at 143.4 mA cm^{-2}) and P-CFCNN (maximally yield 46.2 mW cm^{-2} at 98.7 mA cm^{-2}). Considering that P-CFCNN and 3D CFCNN possessed the same material, it is convictive that the higher discharging performance of 3D CFCNN electrode was resulted from the more abundant three-phase interface ensured by the 3D structure. In addition, this Zn-air battery exhibited long cycling durability: under 10 mA cm^{-2}, it operated more than 300 cycles, totally longer than 110 h. The stable cycling performance also indicated the existed durable three-phase interface. Judging from above water splitting results, the efficient charging process can be ascribed to the high-mass-loaded single-Fe-atom-doped Ni/Ni(OH)$_2$, which afforded high OER catalytic ability.

To reveal the mechanism leading to the high discharging performance, powder-material-based electrodes were prepared to evaluate the ORR performance (Fig. S28), finding that Fe-CNTs played an important role in discharging process. The cross-sectional SEM images of 3D CFCNN electrode (Fig. S29) and powder electrode (Fig. S30) after testing were checked to investigate the permeation of electrolyte during operation. The dispersion of K element (from remaining salt of the electrolyte) in 3D CFCNN exhibited more prominent half-infiltration feature compared with the powder electrode, which reflects the available transport channels of O_2 during discharging process. In addition, the hydrophilia characterization of each component (Fig. S31) declared that, the embedded hydrophobic Fe-CNTs hindered the deep permeation of electrolyte and constructed efficient channel for the transport of O_2. As clarified in Fig. S32, in 3D CFCNN electrode, the outer covered single-Fe-atom-doped Ni/Ni(OH)$_2$ delivered high capability of OER during
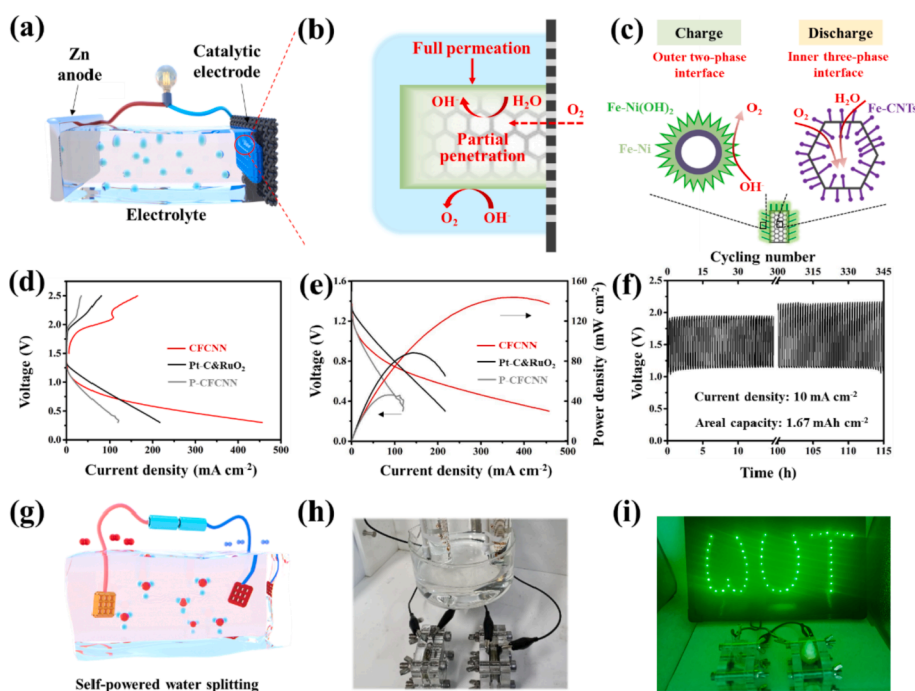
Fig. 5. (a) The schematic illustration of Zn-air battery. (b) Amplified reacting mechanism of ORR/OER and relevant transport channels of O_2. (c) The schematic illustration of active sites of OER and ORR in two-phase interface and triple-phase interface, respectively. (d) The LSV curves of Zn-air battery prepared via CFCNN, P-CFCNN and Pt-C&RuO$_2$ catalyst. (e) The calculated power density at corresponding current densities. (f) Cycling curve of this CFCNN-based Zn-air battery under 10 mA cm^{-2}. (g) The schematic illustration of the self-powered system. (h) The digital photograph of this constructed self-powered system. (i) Two series-connected Zn-air batteries successfully powered LED lamps.

charging, Fe-CNTs embedded in the 3D hierarchical electrode delivered high capability of ORR during discharging, and hydrophilic/hydrophobic interlaced structure resulted in the separated channels for the transport of O_2 and electrolyte. Above three reasons resulted in considerable performance under large current density both in charging and discharging process.

To further verify the practical application, two series-connected Zn-air batteries prepared by CFCNN electrode were applied to power the above OWS vehicle (Fig. 5g). They presented a stable output voltage between 2.8 and 2.9 V (Fig. S33), and the assembled self-powered vehicle delivered an efficient water splitting process (shown in Fig. 5h and recorded as Video 6). Furthermore, they can also successfully power 55 LED lamps (Fig 5i). In addition, the half-wave potential, Charge−discharge voltage gap and peak power density were compared with representative works (shown in Table S2), which reflected the superiority of this work.

From above characterization and test results, the constructed electrodes delivered high performance in water splitting and Zn-air batteries, which shows high correlation with the designed and constructed five-level-synergetic structure (Fig. 6). (1) 3D printing process arose Lev. 1 (Fig. 6a). Benefiting from this digitally controlled process, height of the framework can be easily regulated and pores in the scale of ~ 500 μm can be efficiently fabricated. The thickness of constructed frameworks directly determined the mass loading of subsequently grown active materials. The constructed vertical pores facilitated the rapid release of generated H_2/O_2 during water splitting process [12], and inner periodic channels provided individual path for the infiltration of O_2 in assembled Zn-air batteries [22–26]. (2) The growth of Fe-CNTs arose Lev. 2 (Fig. 6b). Fe-CNTs acted as a highly active catalyst for ORR and played a major role in assembled Zn-air batteries during discharging process. Besides, CNTs with large length/diameter (L/D) ratio tremendously increased the loading mass of deposited Ni/Ni(OH)$_2$ and developed the exposed area to electrolyte, and this one-dimensional structure increased the aerophobic behavior and promoted the release of O_2/H_2 bubbles during water splitting process. Furthermore, Fe particles in CNTs provided Fe source to be doped into Ni/Ni(OH)$_2$ in the following electrodeposition process. (3) Bubble-template electrodeposition of Ni nano-sheets arose Lev. 3 (Fig. 6c). The constructed vertically

aligned Ni nano-sheets further increased the surface area of electrodes, and this coated Ni layer considerably developed electronic conductivity of electrodes and reduced the voltage loss during practical operation. (4) Anode oxidation arose Lev. 4 (Fig. 6d). The surface of Ni nano-sheet was transferred into Ni(OH)$_2$ and a ultrathin coating layer was obtained. This covered layer increased the performance for HER/OER and developed relevant stability. (5) Single-Fe-atom doping of Ni/Ni(OH)$_2$ arose Lev. 5 (Fig. 6e), in which the mix-arrangement of Fe atoms into Ni(OH)$_2$ crystal lattice optimized the structure of electric cloud and immensely enhanced the performance of HER/OER [57,58]. According to above results and the reported works, Fe-doped Ni(OH)$_2$ usually exhibited higher OER performance than Fe-doped Ni when under the similar doping ratio, whereas the latter one exhibited higher HER performance [78]. In addition, Fe-CNTs exhibited higher ORR performance than Fe-doped Ni/Ni(OH)$_2$ [45]. Thus, in this work, it is convincing that, the active species of OER, HER and ORR can be considered to be Fe-doped Ni(OH)$_2$, Fe-doped Ni and Fe-CNTs, respectively. In terms of the fabricating process, each step is highly controllable and aims to efficiently fabricate the electrodes without key difficulty in enlarging the scale. In addition, the finely constructed 3D electrode exhibited remarkable performance. Therefore, the integration of these processes is efficient and meaningful, and the obtained 3D electrode is promising for practical application.

4. Conclusion

Submerged-plant-inspired 3D hierarchical electrodes were constructed and they achieved high performance for trifunctional water electrocatalysis application. Benefiting from the surface single-Fe-atom-doped Ni/Ni(OH)$_2$ active sites and multi-level hierarchical configuration, the electrodes exhibited high performance for OER, HER and overall water splitting. Ascribed to abundant active center in the embedded Fe-CNTs and separated channels for the diffusion of O_2 and electrolyte, the assembled Zn-air battery also delivered considerable performance. In a conclusion, the finely constructed five-level-synergetic hierarchical electrodes and appropriate location of active sites played a crucial role in promoting the performance of OWS and Zn-air batteries. The designing concept and fabricating process of the
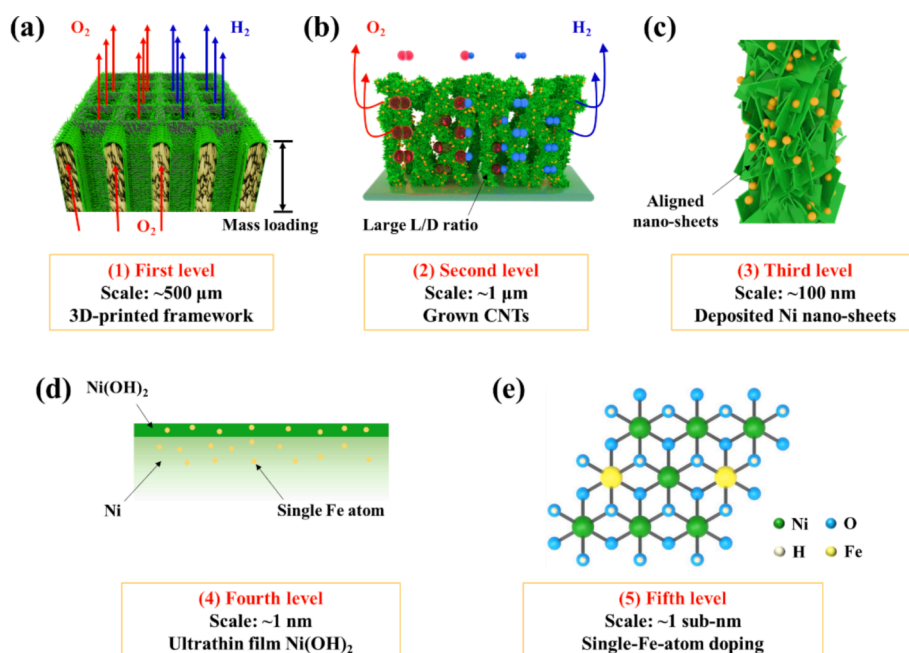

Fig. 6. Schematic illustration of the constructed five-level hierarchical electrode. (a) The first-level structure of 3D-printed framework in the scale of ~ 500 μm. (b) The second-level structure of CNTs in the scale of ~ 1 μm. (c) The third-level structure of Ni nano-sheets in the scale of ~ 100 nm. (d) The fourth-level structure of ultrathin Ni(OH)$_2$ film in the scale of ~ 1 nm. (e) The fifth-level structure of single-atom-Fe doped Ni(OH)$_2$ lattice in the scale of ~ 1 sub-nm.

hierarchical electrodes will pave a new avenue for constructing high-performance trifunctional electrocatalysis electrodes.

Declaration of Competing Interest

The authors declare that they have no known competing financial interests or personal relationships that could have appeared to influence the work reported in this paper.

Acknowledgements

Appendix A. Supplementary data

Supplementary data to this article can be found online at https://doi.org/10.1016/j.cej.2022.136804.

References

[1] X. Cao, Z. Yin, H. Zhang, Three-dimensional graphene materials: preparation, structures and application in supercapacitors, Energy Environ. Sci. 7 (2014) 1850–1865, https://doi.org/10.1039/c4ee00050a.

[2] Y. Luo, Z. Zhang, M. Chhowalla, B. Liu, Recent advances in design of electrocatalysts for high-current-density water splitting, Adv. Mater. 34 (2021) 2108133, https://doi.org/10.1002/adma.202108133.

[3] Y. Ding, B.-Q. Miao, Y.-C. Jiang, H.-C. Yao, X.-F. Li, Y. Chen, Polyethylenimine-modified nickel phosphide nanosheets: interfacial protons boost the hydrogen evolution reaction, J. Mater. Chem. A 7 (2019) 13770–13776, https://doi.org/10.1039/c9ta04283k.

[4] G. Gan, S. Fan, X. Li, J. Wang, C. Bai, X. Guo, M. Tade, S. Liu, Nature of intrinsic defects in carbon materials for electrochemical dechlorination of 1,2-dichloroethane to ethylene, ACS Catal. 11 (2021) 14284–14292, https://doi.org/10.1021/acscatal.1c03701.

[5] D. Li, Y. Qin, J. Liu, H. Zhao, Z. Sun, G. Chen, D.Y. Wu, Y. Su, S. Ding, C. Xiao, Dense crystalline-amorphous interfacial sites for enhanced electrocatalytic oxygen evolution, Adv. Funct. Mater. 32 (2021) 2107056, https://doi.org/10.1002/adfm.202107056.

[6] J.-T. Ren, Y.-S. Wang, L. Chen, L.-J. Gao, W.-W. Tian, Z.-Y. Yuan, Binary FeNi phosphides dispersed on N, P-doped carbon nanosheets for highly efficient overall water splitting and rechargeable Zn-air batteries, Chem. Eng. J. 389 (2020), 124408, https://doi.org/10.1016/j.cej.2020.124408.

[7] Z.-Y. Yuan, Preface to special issue on "Advanced Materials and Catalysis", Front. Chem. Sci. Eng. 15 (6) (2021) 1357–1359, https://doi.org/10.1007/s11705-021-2119-x.

[8] X.-Y. Qin, D. Kin, Y.-Z. Piao, Metal-organic frameworks-derived novel nanostructured electrocatalysts for oxygen evolution, Carbon Energy 3 (2021) 66–100, https://doi.org/10.1002/cey2.80.

[9] Q. Xue, X.-Y. Bai, Y. Zhao, Y.-N. Li, T.-J. Wang, H.-Y. Sun, F.-M. Li, P. Chen, P. Jin, S.-B. Yin, Y. Chen, Au core-PtAu alloy shell nanowires for formic acid electrolysis, Journal of Energy Chemistry 65 (2022) 94–102, https://doi.org/10.1016/j.jechem.2021.05.034.

[10] Y. Li, T. Gao, Y. Yao, Z. Liu, Y. Kuang, C. Chen, J. Song, S. Xu, E.M. Hitz, B. Liu, R. J. Jacob, M.R. Zachariah, G. Wang, L. Hu, In Situ "Chainmail catalyst" assembly in low-tortuosity, hierarchical carbon frameworks for efficient and stable hydrogen generation, Adv. Energy Mater. 8 (2018) 1801289, https://doi.org/10.1002/aenm.201801289.

[11] M. Peng, D. Shi, Y. Sun, J. Cheng, B. Zhao, Y. Xie, J. Zhang, W. Guo, Z. Jia, Z. Liang, L. Jiang, 3D printed mechanically robust graphene/CNT electrodes for highly efficient overall water splitting, Adv. Mater. 32 (2020) 1908201, https://doi.org/10.1002/adma.201908201.

[12] T. Kou, S. Wang, R. Shi, T. Zhang, S. Chiovoloni, J.Q. Lu, W. Chen, M.A. Worsley, B. C. Wood, S.E. Baker, E.B. Duoss, R. Wu, C. Zhu, Y. Li, Periodic Porous 3D Electrodes Mitigate Gas Bubble Traffic during Alkaline Water Electrolysis at High Current Densities, Adv. Energy Mater. 10 (2020) 2002955, https://doi.org/10.1002/aenm.202002955.

[13] C. Liang, P. Zou, A. Nairan, Y. Zhang, J. Liu, K. Liu, S. Hu, F. Kang, H.J. Fan, C. Yang, Exceptional performance of hierarchical Ni–Fe oxyhydroxide@NiFe alloy nanowire array electrocatalysts for large current density water splitting, Energy Environ. Sci. 13 (2020) 86–95, https://doi.org/10.1039/c9ee02388g.

[14] Z. Long, Y. Zhao, C. Zhang, Y. Zhang, C. Yu, Y. Wu, J. Ma, M. Cao, L. Jiang, A multi-bioinspired dual-gradient electrode for microbubble manipulation toward controllable water splitting, Adv. Mater. 32 (2020) 1908099, https://doi.org/10.1002/adma.201908099.

[15] J. Fu, Z.P. Cano, M.G. Park, A. Yu, M. Fowler, Z. Chen, Electrically rechargeable zinc-air batteries: progress, challenges, and perspectives, Adv. Mater. 29 (2017) 1604685, https://doi.org/10.1002/adma.201604685.

[16] J. Fu, R. Liang, G. Liu, A. Yu, Z. Bai, L. Yang, Z. Chen, Recent Progress in Electrically Rechargeable Zinc-Air Batteries, Adv. Mater. 31 (2019) 1805230, https://doi.org/10.1002/adma.201805230.

[17] A. Sumboja, B. Prakoso, Y. Ma, F.R. Irwan, J.J. Hutani, A. Mulyadewi, M.A. A. Mahbub, Y. Zong, Z. Liu, FeCo nanoparticle-loaded nutshell-derived porous carbon as sustainable catalyst in Al-air batteries, Energy Material Advances 2021 (2021) 1–12, https://doi.org/10.34133/2021/7386210.

[18] C.-C. Weng, J.-T. Ren, H.-Y. Wang, X.-W. Lv, Y.-J. Song, Y.-S. Wang, L. Chen, W.-W. Tian, Z.-Y. Yuan, Triple-phase oxygen electrocatalysis of hollow spherical structures for rechargeable Zn-Air batteries, Appl. Catal. B 307 (2022), 121190, https://doi.org/10.1016/j.apcatb.2022.121190.

[19] S. Dou, C.L. Dong, Z. Hu, Y.C. Huang, J.l. Chen, L. Tao, D. Yan, D. Chen, S. Shen, S. Chou, S. Wang, Atomic-Scale CoOₓ Species in Metal–Organic Frameworks for Oxygen Evolution Reaction, Adv. Funct. Mater. 27 (2017) 1702546, https://doi.org/10.1002/adfm.201702546.

[20] W.H. Lai, L. Zhang, Z. Yan, W. Hua, S. Indris, Y. Lei, H. Liu, Y.X. Wang, Z. Hu, H. K. Liu, S. Chou, G. Wang, S.X. Dou, Activating inert surface pt single atoms via subsurface doping for oxygen reduction reaction, Nano Lett. 21 (2021) 7970–7978, https://doi.org/10.1021/acs.nanolett.1c02013.

[21] T.Y. Jeon, S.H. Yu, S.J. Yoo, H.Y. Park, S.K. Kim, Electrochemical determination of the degree of atomic surface roughness in Pt–Ni alloy nanocatalysts for oxygen reduction reaction, Carbon Energy 3 (2020) 375–383, https://doi.org/10.1002/cey2.82.

[22] S.D. Lacey, D.J. Kirsch, Y. Li, J.T. Morgenstern, B.C. Zarket, Y. Yao, J. Dai, L. Q. Garcia, B. Liu, T. Gao, S. Xu, S.R. Raghavan, J.W. Connell, Y. Lin, L. Hu, Extrusion-based 3D printing of hierarchically porous advanced battery electrodes, Adv. Mater. 30 (2018) 1705651, https://doi.org/10.1002/adma.201705651.

[23] X. Lin, J. Wang, X. Gao, S. Wang, Q. Sun, J. Luo, C. Zhao, Y. Zhao, X. Yang, C. Wang, R. Li, X. Sun, 3D printing of free-standing "O₂ breathable" air electrodes for high-capacity and long-life Na–O₂ batteries, Chem. Mater. 32 (2020) 3018–3027, https://doi.org/10.1021/acs.chemmater.9b05360.

[24] Z. Lyu, G.J.H. Lim, R. Guo, Z. Kou, T. Wang, C. Guan, J. Ding, W. Chen, J. Wang, 3D-Printed MOF-derived hierarchically porous frameworks for practical high-energy density Li-O₂ Batteries, Adv. Funct. Mater. 29 (2019) 1806658, https://doi.org/10.1002/adfm.201806658.

[25] Y. Qiao, Y. Liu, C. Chen, H. Xie, Y. Yao, S. He, W. Ping, B. Liu, L. Hu, 3D-printed graphene oxide framework with thermal shock synthesized nanoparticles for Li-CO₂ Batteries, Adv. Funct. Mater. 28 (2018) 1805899, https://doi.org/10.1002/adfm.201805899.

[26] J. Zhang, X.L. Li, S. Fan, S. Huang, D. Yan, L. Liu, P. Valdivia y Alvarado, H. Y. Yang, 3D-printed functional electrodes towards Zn-Air batteries, Mater. Today Energy 16 (2020) 100407, https://doi.org/10.1016/j.mtener.2020.100407.

[27] M.S. Faber, S. Jin, Earth-abundant inorganic electrocatalysts and their nanostructures for energy conversion applications, Energy Environ. Sci. 7 (2014) 3519–3542, https://doi.org/10.1039/c4ee01760a.

[28] Q. Qin, H. Jang, L. Chen, G. Nam, X. Liu, J. Cho, Low loading of RhₓP and RuP on N, P codoped carbon as two trifunctional electrocatalysts for the oxygen and hydrogen electrode reactions, Adv. Energy Mater. 8 (2018) 1801478, https://doi.org/10.1002/aenm.201801478.

[29] H. Zhu, J. Zhang, R. Yanzhang, M. Du, Q. Wang, G. Gao, J. Wu, G. Wu, M. Zhang, B. Liu, J. Yao, X. Zhang, When cubic cobalt sulfide meets layered molybdenum disulfide: a core-shell system toward synergetic electrocatalytic water splitting, Adv. Mater. 27 (2015) 4752–4759, https://doi.org/10.1002/adma.201501969.

[30] O. Pedersen, T.D. Colmer, K. Sand-Jensen, Underwater photosynthesis of submerged plants-recent advances and methods, Front Plant Sci. 4 (2013) 140, https://doi.org/10.3389/fpls.2013.00140.

[31] A.J. Ragauskas, C.K. Williams, B.H. Davison, G. Britovsek, J. Cairney, C.A. Eckert, W.J. Frederick Jr., J.P. Hallett, D.J. Leak, C.L. Liotta, J.R. Mielenz, R. Murphy, R. Templer, T. Tschaplinski, The path forward for biofuels and biomaterials, Science 311 (2006) 484–489, https://doi.org/10.1126/science.1114736.

[32] I. Herraiz-Cardona, E. Ortega, L. Vázquez-Gómez, V. Pérez-Herranz, Double-template fabrication of three-dimensional porous nickel electrodes for hydrogen evolution reaction, Int. J. Hydrogen Energy 37 (2012) 2147–2156, https://doi.org/10.1016/j.ijhydene.2011.09.155.

[33] X. Yu, M. Wang, Z. Wang, X. Gong, Z. Guo, The structure evolution mechanism of electrodeposited porous Ni films on NH₄Cl concentration, Appl. Surf. Sci. 360 (2016) 502–509, https://doi.org/10.1016/j.apsusc.2015.10.174.

[34] X. Yu, J. Yang, Z. Sui, M. Wang, Effects of ultrasonic field on structure evolution of Ni film electrodeposited by bubble template method for hydrogen evolution electrocatalysis, J. Solid State Electrochem. 25 (2021) 2201–2212, https://doi.org/10.1007/s10008-021-04980-4.

[35] R.D. Farahani, M. Dube, D. Therriault, Three-dimensional printing of multifunctional nanocomposites: manufacturing techniques and applications, Adv. Mater. 28 (2016) 5794–5821, https://doi.org/10.1002/adma.201506215.

[36] H. Li, J. Liang, Recent Development of Printed Micro-Supercapacitors: Printable Materials, Printing Technologies, and Perspectives, Adv. Mater. 32 (2020) 1805864, https://doi.org/10.1002/adma.201805864.

[37] D. Cao, Y. Xing, K. Tantratian, X. Wang, Y. Ma, A. Mukhopadhyay, Z. Cheng, Q. Zhang, Y. Jiao, L. Chen, H. Zhu, 3D printed high-performance lithium metal microbatteries enabled by nanocellulose, Adv. Mater. 31 (2019) 1807313, https://doi.org/10.1002/adma.201807313.

[38] S. Sultan, H.N. Abdelhamid, X. Zou, A.P. Mathew, CelloMOF: nanocellulose enabled 3D printing of metal-organic frameworks, Adv. Funct. Mater. 29 (2019) 1805372, https://doi.org/10.1002/adfm.201805372.

[39] W. Chen, H. Yu, S.Y. Lee, T. Wei, J. Li, Z. Fan, Nanocellulose: a promising nanomaterial for advanced electrochemical energy storage, Chem. Soc. Rev. 47 (2018) 2837–2872, https://doi.org/10.1039/C7CS00790F.

[40] Z.Y. Wu, H.W. Liang, B.C. Hu, S.H. Yu, Emerging carbon-nanofiber aerogels: chemosynthesis versus biosynthesis, Angew Chem Int Ed Engl. 57 (2018) 15646–15662, https://doi.org/10.1002/anie.201802663.

[41] K. Fu, Y. Wang, C. Yan, Y. Yao, Y. Chen, J. Dai, S. Lacey, Y. Wang, J. Wan, T. Li, Z. Wang, Y. Xu, L. Hu, Graphene oxide-based electrode inks for 3D-printed lithium-ion batteries, Adv. Mater. 28 (2016) 2587–2594, https://doi.org/10.1002/adma.201505391.

[42] Y. Jiang, Z. Xu, T. Huang, Y. Liu, F. Guo, J. Xi, W. Gao, C. Gao, Direct 3D Printing of Ultralight Graphene Oxide Aerogel Microlattices, Adv. Funct. Mater. 28 (2018) 1707024, https://doi.org/10.1002/adfm.201707024.

[43] H. Liu, Y. Zhang, R. Li, X. Sun, S. Désilets, H. Abou-Rachid, M. Jaidann, L.-S. Lussier, Structural and morphological control of aligned nitrogen-doped carbon nanotubes, Carbon 48 (2010) 1498–1507, https://doi.org/10.1016/j.carbon.2009.12.045.

[44] M. Terrones, H. Terrones, N. Grobert, W.K. Hsu, Y.Q. Zhu, J.P. Hare, H.W. Kroto, D. R.M. Walton, P. Kohler-Redlich, M. Rühle, J.P. Zhang, A.K. Cheetham, Efficient route to large arrays of CNx nanofibers by pyrolysis of ferrocene/melamine mixtures, Appl. Phys. Lett. 75 (1999) 3932–3934, https://doi.org/10.1063/1.125498.

[45] D. Xia, D. Yang, L. Xie, Y. Wei, W. Jiang, M. Dou, X. Li, J. Li, L. Gan, F. Kang, Direct Growth of Carbon Nanotubes Doped with Single Atomic Fe–N₄ Active Sites and Neighboring Graphitic Nitrogen for Efficient and Stable Oxygen Reduction Electrocatalysis, Adv. Funct. Mater. 29 (2019) 1906174, https://doi.org/10.1002/adfm.201906174.

[46] C.J. Lee, J. Park, J.A.J.C.P.L. Yu, Catalyst effect on carbon nanotubes synthesized by thermal chemical vapor deposition, Chem. Phys. Lett. 360 (2002) 250–255, https://doi.org/10.1016/s0009-2614(02)00831-x.

[47] S. Zhang, M. Jin, T. Shi, M. Han, Q. Sun, Y. Lin, Z. Ding, L.R. Zheng, G. Wang, Y. Zhang, H. Zhang, H. Zhao, Electrocatalytically active Fe-(O-C₂)₄ Single-atom sites for efficient reduction of nitrogen to ammonia, Angew Chem Int Ed Engl. 59 (2020) 13423–13429, https://doi.org/10.1002/anie.202005930.

[48] Z. Hao, L. Xu, Q. Liu, W. Yang, X. Liao, J. Meng, X. Hong, L. He, L. Mai, On-Chip Ni–Zn microbattery based on hierarchical ordered porous Ni@Ni(OH)₂ microelectrode with ultrafast ion and electron transport kinetics, Adv. Funct. Mater. 29 (2019) 1808470, https://doi.org/10.1002/adfm.201808470.

[49] P. Liu, B. Chen, C. Liang, W. Yao, Y. Cui, S. Hu, P. Zou, H. Zhang, H.J. Fan, C. Yang, Tip-enhanced electric field: A new mechanism promoting mass transfer in oxygen evolution reactions, Adv. Mater. 33 (2021) 2007377, https://doi.org/10.1002/adma.202007377.

[50] W. Li, S. Li, A.A. Bernussi, Z. Fan, 3-D edge-oriented electrocatalytic NiCo₂S₄ nanoflakes on vertical graphene for Li-S batteries, Energy Material Advances 2021 (2021) 1–11, https://doi.org/10.34133/2021/2712391.

[51] Y. Dou, C.-T. He, L. Zhang, M. Al-Mamun, H. Guo, W. Zhang, Q. Xia, J. Xu, L. Jiang, Y. Wang, P. Liu, X.-M. Chen, H. Yin, H. Zhao, How cobalt and iron doping determine the oxygen evolution electrocatalytic activity of NiOOH, Cell Reports Physical Science 1 (2020) 100077, https://doi.org/10.1016/j.xcrp.2020.100077.

[52] Z. Zeng, L.Y. Gan, H. Bin Yang, X. Su, J. Gao, W. Liu, H. Matsumoto, J. Gong, J. Zhang, W. Cai, Z. Zhang, Y. Yan, B. Liu, P. Chen, Orbital coupling of hetero-diatomic nickel-iron site for bifunctional electrocatalysis of CO₂ reduction and oxygen evolution, Nat. Commun. 12 (2021) 4088, https://doi.org/10.1038/s41467-021-24052-5.

[53] K. Yuan, D. Lutzenkirchen-Hecht, L. Li, L. Shuai, Y. Li, R. Cao, M. Qiu, X. Zhuang, M.K.H. Leung, Y. Chen, U. Scherf, Boosting oxygen reduction of single iron active sites via geometric and electronic engineering: nitrogen and phosphorus dual coordination, J. Am. Chem. Soc. 142 (2020) 2404–2412, https://doi.org/10.1021/jacs.9b11852.

[54] Z. Jin, P. Li, Y. Meng, Z. Fang, D. Xiao, G. Yu, Understanding the inter-site distance effect in single-atom catalysts for oxygen electroreduction, Nature Catalysis 4 (2021) 615–622, https://doi.org/10.1038/s41929-021-00650-w.

[55] J. Li, M. Chen, D.A. Cullen, S. Hwang, M. Wang, B. Li, K. Liu, S. Karakalos, M. Lucero, H. Zhang, C. Lei, H. Xu, G.E. Sterbinsky, Z. Feng, D. Su, K.L. More, G. Wang, Z. Wang, G. Wu, Atomically dispersed manganese catalysts for oxygen reduction in proton-exchange membrane fuel cells, Nature Catalysis 1 (2018) 935–945, https://doi.org/10.1038/s41929-018-0164-8.

[56] L. Zhao, Y. Zhang, L.B. Huang, X.Z. Liu, Q.H. Zhang, C. He, Z.Y. Wu, L.J. Zhang, J. Wu, W. Yang, L. Gu, J.S. Hu, L.J. Wan, Cascade anchoring strategy for general mass production of high-loading single-atomic metal-nitrogen catalysts, Nat. Commun. 10 (2019) 1278, https://doi.org/10.1038/s41467-019-09290-y.

[57] S. Klaus, Y. Cai, M.W. Louie, L. Trotochaud, A.T. Bell, Effects of Fe Electrolyte Impurities on Ni(OH)₂/NiOOH Structure and Oxygen Evolution Activity, J. Phys. Chem. C 119 (2015) 7243–7254, https://doi.org/10.1021/acs.jpcc.5b00105.

[58] L. Trotochaud, S.L. Young, J.K. Ranney, S.W. Boettcher, Nickel-iron oxyhydroxide oxygen-evolution electrocatalysts: the role of intentional and incidental iron incorporation, J. Am. Chem. Soc. 136 (2014) 6744–6753, https://doi.org/10.1021/ja502379c.

[59] Q. Qian, Y. Li, Y. Liu, L. Yu, G. Zhang, Ambient fast synthesis and active sites deciphering of hierarchical foam-like trimetal-organic framework nanostructures as a platform for highly efficient oxygen evolution electrocatalysis, Adv. Mater. 31 (2019) 1901139, https://doi.org/10.1002/adma.201901139.

[60] F. Yu, H. Zhou, Y. Huang, J. Sun, F. Qin, J. Bao, W.A. Goddard III, S. Chen, Z. Ren, High-performance bifunctional porous non-noble metal phosphide catalyst for overall water splitting, Nat. Commun. 9 (2018) 2551, https://doi.org/10.1038/s41467-018-04746-z.

[61] L.-G. He, P.-Y. Cheng, C.-C. Cheng, C.-L. Huang, C.-T. Hsieh, S.-Y. Lu, (NiₓFeyCo6-x-y)Mo₆C cuboids as outstanding bifunctional electrocatalysts for overall water splitting, Appl. Catal. B 290 (2021) 0926, https://doi.org/10.1016/j.apcatb.2021.120049.

[62] L. Wu, L. Yu, F. Zhang, B. McElhenny, D. Luo, A. Karim, S. Chen, Z. Ren, Heterogeneous bimetallic phosphide Ni₂P-Fe₂P as an efficient bifunctional catalyst for water/seawater splitting, Adv. Funct. Mater. 31 (2020) 2006484, https://doi.org/10.1002/adfm.202006484.

[63] Y. Wu, X. Tao, Y. Qing, H. Xu, F. Yang, S. Luo, C. Tian, M. Liu, X. Lu, Cr-Doped FeNi-P nanoparticles encapsulated into N-doped carbon nanotube as a robust bifunctional catalyst for efficient overall water splitting, Adv. Mater. 31 (2019) 1900178, https://doi.org/10.1002/adma.201900178.

[64] Y. Guo, J. Tang, Z. Wang, Y.-M. Kang, Y. Bando, Y. Yamauchi, Elaborately assembled core-shell structured metal sulfides as a bifunctional catalyst for highly efficient electrochemical overall water splitting, Nano Energy 47 (2018) 494–502, https://doi.org/10.1016/j.nanoen.2018.03.012.

[65] Y. Li, H. Zhang, M. Jiang, Q. Zhang, P. He, X. Sun, 3D self-supported Fe-Doped Ni₂P nanosheet arrays, Adv. Funct. Mater. 27 (2017) 1702513, https://doi.org/10.1002/adfm.201702513.

[66] R.-Q. Li, B.-L. Wang, T. Gao, R. Zhang, C. Xu, X. Jiang, J. Zeng, Y. Bando, P. Hu, Y. Li, X.-B. Wang, Monolithic electrode integrated of ultrathin NiFeP on 3D strutted graphene for bifunctionally efficient overall water splitting, Nano Energy 58 (2019) 870–876, https://doi.org/10.1016/j.nanoen.2019.02.024.

[67] M. Li, Y. Zhu, H. Wang, C. Wang, N. Pinna, X. Lu, Ni strongly coupled with mo₂c encapsulated in nitrogen-doped carbon nanofibers as robust bifunctional catalyst for overall water splitting, Adv. Energy Mater. 9 (2019) 1803185, https://doi.org/10.1002/aenm.201803185.

[68] L. Yan, Y. Xu, P. Chen, S. Zhang, H. Jiang, L. Yang, Y. Wang, L. Zhang, J. Shen, X. Zhao, L. Wang, A Freestanding 3D Heterostructure Film Stitched by MOF-Derived Carbon Nanotube Microsphere Superstructure and Reduced Graphene Oxide Sheets: A Superior Multifunctional Electrode for Overall Water Splitting and Zn-Air Batteries, Adv. Mater. 32 (2020) 2003313, https://doi.org/10.1002/adma.202003313.

[69] Z. Chen, Y. Ha, H. Jia, X. Yan, M. Chen, M. Liu, R. Wu, Oriented transformation of Co-LDH into 2D/3D ZIF-67 to Achieve Co–N–C hybrids for efficient overall water splitting, Adv. Energy Mater. 9 (2019) 1803918, https://doi.org/10.1002/aenm.201803918.

[70] L. Huang, D. Chen, G. Luo, Y.R. Lu, C. Chen, Y. Zou, C.L. Dong, Y. Li, S. Wang, Zirconium-regulation-induced bifunctionality in 3D cobalt-iron oxide nanosheets for overall water splitting, Adv. Mater. 31 (2019) 1901439, https://doi.org/10.1002/adma.201901439.

[71] W. Gan, L. Wu, Y. Wang, H. Gao, L. Gao, S. Xiao, J. Liu, Y. Xie, T. Li, J. Li, Carbonized Wood Decorated with Cobalt-Nickel Binary Nanoparticles as a Low-Cost and Efficient Electrode for Water Splitting, Adv. Funct. Mater. 31 (2021) 2010951, https://doi.org/10.1002/adfm.202010951.

[72] M. Li, H. Wang, W. Zhu, W. Li, C. Wang, X. Lu, RuNi nanoparticles embedded in N-doped carbon nanofibers as a robust bifunctional catalyst for efficient overall water splitting, Adv. Sci. 7 (2020) 1901833, https://doi.org/10.1002/advs.201901833.

[73] W. Zhang, Q. Jia, H. Liang, L. Cui, D. Wei, J. Liu, Iron doped Ni₃S₂ nanorods directly grown on FeNi₃ foam as an efficient bifunctional catalyst for overall water splitting, Chem. Eng. J. 396 (2020), 125315, https://doi.org/10.1016/j.cej.2020.125315.

[74] H. Liu, X. Li, L. Chen, X. Zhu, P. Dong, M.O.L. Chee, M. Ye, Y. Guo, J. Shen, Monolithic Ni-Mo-B bifunctional electrode for large current water splitting, Adv. Funct. Mater. 32 (2021) 2107308, https://doi.org/10.1002/adfm.202107308.

[75] C. Hu, L. Zhang, Z.J. Zhao, A. Li, X. Chang, J. Gong, synergism of geometric construction and electronic regulation: 3D Se-(NiCo)Sₓ/(OH)ₓ nanosheets for highly efficient overall water splitting, Adv. Mater. 30 (2018) 1705538, https://doi.org/10.1002/adma.201705538.

[76] L. Yu, H. Zhou, J. Sun, F. Qin, F. Yu, J. Bao, Y. Yu, S. Chen, Z. Ren, Cu nanowires shelled with NiFe layered double hydroxide nanosheets as bifunctional electrocatalysts for overall water splitting, Energy Environ. Sci. 10 (2017) 1820–1827, https://doi.org/10.1039/c7ee01571b.

[77] T. Tang, W.J. Jiang, S. Niu, N. Liu, H. Luo, Y.Y. Chen, S.F. Jin, F. Gao, L.J. Wan, J. S. Hu, Electronic and morphological dual modulation of cobalt carbonate hydroxides by Mn doping toward highly efficient and stable bifunctional electrocatalysts for overall water splitting, J. Am. Chem. Soc. 139 (2017) 8320–8328, https://doi.org/10.1021/jacs.7b03507.

[78] V. Vij, S. Sultan, A.M. Harzandi, A. Meena, J.N. Tiwari, W.-G. Lee, T. Yoon, K. S. Kim, Nickel-based electrocatalysts for energy-related applications: oxygen reduction, oxygen evolution, and hydrogen evolution reactions, ACS Catal. 7 (2017) 7196–7225, https://doi.org/10.1021/acscatal.7b01800.